Cement and Concrete Research 68 (2015) 94–104

Contents lists available at ScienceDirect

Cement and Concrete Research

journal homepage: http://ees.elsevier.com/CEMCON/default.asp

Tensile Rate Effects in High Strength-High Ductility Concrete

Ravi Ranade [a], Victor C. Li [b,*], William F. Heard [c]

[a] Institute of Bridge Engineering, Department of Civil, Structural, and Environmental Engineering, State University of New York at Buffalo, 135 Ketter Hall, Buffalo, NY 14260, USA
[b] Department of Civil and Environmental Engineering, University of Michigan Ann Arbor, 2350 Hayward St, Ann Arbor, MI 48109, USA
[c] US Army Engineer Research and Development Center (ERDC), 3909 Halls Ferry Rd, Bldg 5028, Vicksburg, MS 39180, USA

ARTICLE INFO

Article history:
Received 12 June 2014
Accepted 10 November 2014
Available online xxxx

Keywords:
Strain effect
Mechanical properties
Micromechanics
High-performance concrete
Composite

ABSTRACT

Researchers at the University of Michigan have recently developed a new class of concrete, named High Strength-High Ductility Concrete (HSHDC), which possesses exceptional combination of compressive strength (>150 MPa) and tensile ductility (>3%) under quasi-static loads. The structural applications of HSHDC for withstanding extreme events, such as hurricanes, earthquakes, impacts, and blasts, require an understanding of its dynamic behavior at high strain rates. This research experimentally investigates the effects of strain rate (from 10^{-4}/s to 10/s) on the composite tensile properties and the micro-scale fiber/matrix interaction properties of HSHDC. A micromechanics-based scale-linking model is used to analytically explain the composite-scale rate effects based on the micro-scale rate effects. Due to the unique interactions between the Polyethylene fibers and densely packed ultra-high strength matrix of HSHDC, novel rate effects are revealed, which are expected to be foundational for the future development of this class of materials for improving infrastructure resilience.

1. Introduction

A new fiber-reinforced cementitious composite (FRCC), named High Strength-High Ductility Concrete (HSHDC) [1,2], has been recently developed at the University of Michigan in collaboration with the Engineer Research and Development Center (ERDC) of the US Army Corps of Engineers. Under quasi-static loads, HSHDC exhibits a unique combination of ultra-high compressive strength (greater than 150 MPa) and ultra-high tensile ductility (greater than 3% under direct tension). Such properties point toward the potential of utilizing HSHDC in structures subjected to high-energy dynamic loadings, such as impacts, blasts, hurricanes, and earthquakes; however, the behavior of HSHDC at high strain rates is so far unknown, which is the motivation behind this study.

The effects of load/strain rate on the mechanical properties, particularly strength and modulus, of normal and high-strength concretes have been widely reported in the literature [3–14]. The rate of increase in the dynamic strength of concrete with strain rate under tension is almost 2–3 times that of under compression. These observed rate effects are typically formulated as bilinear functions similar to that given in the CEB-FIP code [15]. Although a similar bilinear trend of increase in the dynamic strength with the logarithm of strain rate is observed for high strength concretes, the rates of increase are smaller in high strength concretes than that of normal concrete [16,17].

Significant research exists on investigating the plausible causes of the rate effects in concrete at various length scales. The macroscopic explanation of the rate sensitivity of concrete properties is based on comparing the crack propagation velocity with the Rayleigh wave velocity, and its implications on the apparent fracture toughness [18–20]. The meso-scale (size of aggregate) explanation is based on the observations of cracks cutting through the aggregates, instead of meandering around them along the weak aggregate-hardened cement paste interface [21–23], at high strain rates. This occurs due to both high stresses in the material at high strain rates and the inertia of the material elements besides the surface of the rapidly growing crack [21]. Greater toughness of the aggregates than the interface leads to higher material toughness and, therefore, larger dynamic strength. At nano-/micro-scales, the crack growth is considered as breakage of bonds between two particles governed by thermodynamics. At high strain rates, the material shows higher resistance to crack propagation as it fails to respond thermodynamically as fast as the strain change (thermal inertia) [24]. Each of the above theories explaining the rate sensitivity of concrete's properties is applicable over a limited range of strain rates, and it is plausibly the combined effect of some or all of these theories that leads to the observed change in the mechanical properties, particularly strength and modulus, of concrete with the strain rate.

The presence of fibers in FRCCs adds more degrees of complexity to the material behavior at high strain rates, particularly under tension [25,26]. The hydrophilic polymer fibers in FRCCs form both chemical and frictional bonds with the cementitious matrix. The chemical bond between the fibers and the cementitious matrix is highly rate-sensitive and significantly increases at high strain-rates, which influences the tensile ductility and other composite mechanical properties [27–29]. Compared to the chemical bond, the frictional

* Corresponding author.
E-mail address: vcli@umich.edu (V.C. Li).

http://dx.doi.org/10.1016/j.cemconres.2014.11.005
0008-8846/

bond between the fibers and the cementitious matrix is less sensitive to strain rate [30–32]. Steel fibers and hydrophobic polymer fibers only form a frictional bond with the FRCC's cementitious matrix and, therefore, the rate effects on the fiber-bridging are less severe in such composites. However, the increase in fiber/matrix frictional bond can be significant for very high volume fraction of fibers (>10%) [33]. In addition to the interfacial bond, the rate effects on the fiber properties also influence the rate effects on the composite properties. For instance, while the polymer fibers are highly rate-sensitive due to their viscoelastic behavior, steel fibers are largely insensitive to strain rate [34,35]. Thus, the composite-scale rate effects on the tensile properties of FRCCs are greatly influenced by the micro-scale rate effects on the fiber/matrix bond and fiber properties, in addition to the rate effects on the matrix fracture toughness [27].

HSHDC, investigated in this study, is a strain-hardening FRCC containing an ultra-high strength cementitious matrix and hydrophobic ultra-high molecular weight polyethylene (UHMWPE) fibers; henceforth, referred as PE fibers. The objectives of the research presented in this paper are: (1) to investigate the influence of strain rates (from 10^{-4}/s to 10/s) on the composite-scale direct tension behavior of HSHDC. (The influence of strain rate on the compressive behavior of HSHDC is beyond the scope of this paper, and it will be investigated in a future study.), (2) to determine the influence of strain rate on the micro-scale fiber/matrix interaction properties and matrix fracture toughness of HSHDC, and (3) to investigate whether the micro-scale rate effects explain the composite-scale rate effects through analytical investigation of the fiber-bridging behavior.

In the following sections, first, the details of the experimental investigations, for determining the rate effects on the composite and micro-scale properties of HSHDC, are presented. While the direct tension tests on dogbone-shaped specimens are used to determine the composite tensile behavior of HSHDC at various strain rates, single fiber pullout tests, in combination with the micromechanics-based analytical models, are used to determine the micro-scale fiber/matrix interaction properties and fiber properties at the corresponding displacement rates. Statistical scale-linking model, taking into account the randomness in fiber distribution and fiber embedment lengths, are then used to predict the composite-scale rate effects based on the observed micro-scale rate effects. The predicted rate effects are finally compared with the experimentally observed rate effects at the composite scale, thus providing crucial insights into the material behavior at both these length-scales under dynamic loads.

2. Research significance

Besides adding significantly to the limited knowledge of the tensile rate effects in strain-hardening FRCCs, this research specifically provides insights into the influence of strain rate on the bond between polyethylene fibers and a cementitious matrix. Although other polymer fibers and steel fibers have been investigated in a limited number of studies, the rate effects on a PE fiber-reinforced FRCC, particularly with such ultra-high strength matrix, have never been examined before this study. The micro-scale rate effects on the bond between the PE fiber and the cementitious matrix, along with the rate effects on the fiber and matrix properties, uniquely influence the composite tensile properties of HSHDC at high strain rates, and this scale linkage is clearly illuminated in this study through analytical modeling. While the experimental data on the composite behavior of HSHDC at high strain rates generated in this study is useful for exploring its structural applications, the micro-scale properties of HSHDC at high rates provide crucial guidance for continued micromechanics-based tailoring of this material for achieving the desired structural performance.

3. Experimental investigation

3.1. Materials and specimens

Similar to other high performance concretes, HSHDC consists of cementitious materials (cement and silica fume), fine aggregates, water, and a High-Range Water-Reducing Admixture (HRWRA), along with the PE fibers. The mix proportions along with the particle size and weights of constituents per unit volume of the composite are given in Table 1. Further details about the constituent materials are given by Ranade et al. [1].

Three types of specimens were cast in this study: (1) planar dogbone specimens made of HSHDC composite, (2) single fiber pullout specimens with PE fibers embedded in HSHDC matrix, and (3) beam specimens (notched after curing) of HSHDC matrix (without fibers) for fracture toughness measurement. The geometry and preparation of the dogbone specimens of HSHDC are described by Ranade et al. [1], and that of the single fiber pullout specimens and the beam specimens for matrix fracture toughness measurements are described by Ranade et al. [2]. In this study, six dogbone specimens, twenty-five single fiber pullout specimens, and four notched beams were tested for each strain rate to reliably determine the average properties and their variations at composite- and micro-scales. All specimens were cured following the *HSHDC curing procedure* described by Ranade et al. [1].

Out of the twenty-five single fiber pullout specimens cast in this study for each strain rate, ten specimens were cast with fibers aligned with the loading direction to measure the interfacial bond properties, whereas five specimens were cast with fibers inclined at 27° [$\tan^{-1}(1/2)$] and another five with fibers inclined at 45° ($\tan^{-1}1$) to quantify the effects of snubbing and inclination hardening on the inclined fibers. The remaining five specimens were cast with embedment lengths exceeding 15 mm to determine the PE fiber's in-situ strength and modulus. Further details regarding the choice of angles and number of specimens are given by Ranade et al. [2].

3.2. Experimental procedures

The direct tension tests on the dogbone specimens were performed at six different tensile strain rates: $10^{-4}\ s^{-1}$, $10^{-3}\ s^{-1}$, $10^{-2}\ s^{-1}$, $10^{-1}\ s^{-1}$, $1\ s^{-1}$, and $10\ s^{-1}$ by applying controlled tensile displacement rates (gauge length of 90 mm) of 9 μm/s, 90 μm/s, 0.9 mm/s, 9 mm/s, 90 mm/s, and 0.9 m/s, respectively. These tests were performed on an electro-mechanical tensile test system with the maximum load capacity of 10 kN. The test setup for the direct tension tests is shown in Fig. 1a. A lost motion grip assembly was used for all the tests conducted at displacement rates greater than 1 mm/s. The 'gap' shown in this assembly (Fig. 1b) is set such that the actuator of the tensile test system achieves the desired displacement rate before engaging the specimen. While the built-in dynamic load cell (with range of 25 kN) of the test system was used to determine the tensile stress from the measured tensile force, the corresponding tensile strain in a dogbone specimen was determined from the average of the displacements measured by the two LVDTs mounted on either side of the specimen. The data (both tensile force

Table 1
Mix proportions of HSHDC.

Constituent	Particle size (μm)	Weight relative to cement	Weight per unit volume, kg/m^3
Class H cement	30–80	1	907
Silica fume	0.1–1	0.389	353
Silica flour	5–100	0.277	251
Silica sand	100–600	0.700	635
Tap water	–	0.208 w/cm = 0.15	189
HRWRA	–	0.018	16
PE fiber	–	0.0214	19

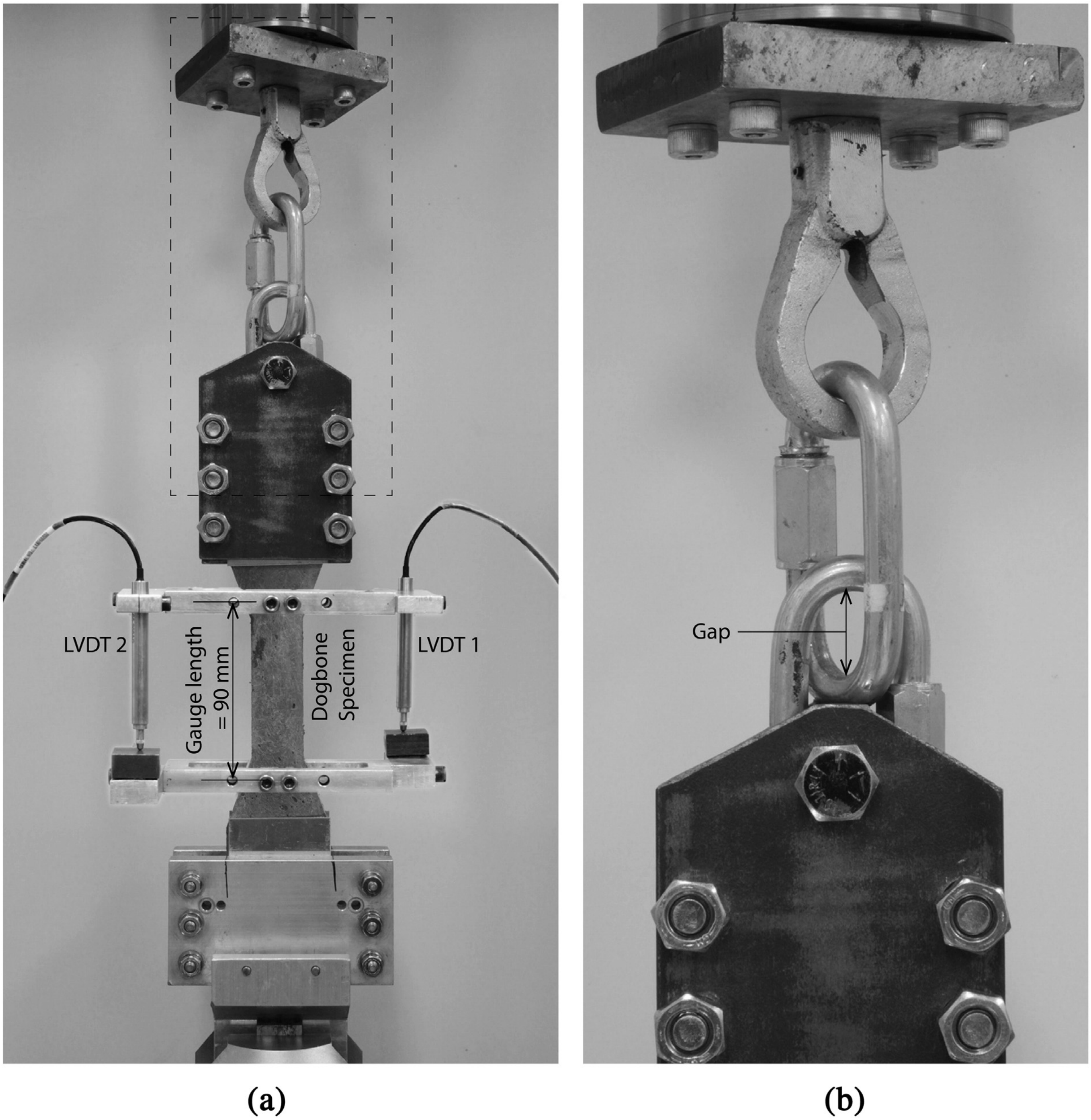

Fig. 1. Direct tension test setup (a) entire setup and (b) zoomed view of the lost-motion assembly.

and displacement) was recorded at the rate of 10^4 times the applied strain rate for a given test.

The single fiber pullout tests were conducted at the six tensile displacement rates (9 μm/s to 0.9 m/s) using the 10 kN test system, same as that used for the direct tension tests. The procedure for the single fiber pullout tests is described in detail by Ranade et al. [2]. Similar to the direct tension tests, the lost motion assembly was used for the two fastest displacement rates.

The fracture toughness tests were conducted at only four (instead of six) compressive displacement rates of 20 μm/s, 0.2 mm/s, 2 mm/s, and 10 mm/s. The notched beams used for the fracture toughness tests are too bulky for the 10 kN system mentioned above and, therefore, a 100 kN hydraulic test system was used to perform the fracture toughness tests. However, the maximum achievable displacement rate with the 100 kN test system is 10 mm/s. The first three compressive displacement rates ($d\Delta/dt = 20$ μm/s, 0.2 mm/s, and 2 mm/s) provide an effective tensile strain rate ($d\varepsilon/dt$ defined as $(6d/L^2)$. $d\Delta/dt$ from the elastic flexure theory, with $L = 254$ mm; $d = 46.2$ mm [36]) of approximately $10^{-4}\ s^{-1}$, $10^{-3}\ s^{-1}$, and $10^{-2}\ s^{-1}$ (same as the first three strain rates for direct tension tests) at the notch tip, and the compressive displacement rate of 10 mm/s is equivalent to the tensile strain rate about 0.05/s.

4. Experimental results and discussion

4.1. Composite behavior

One representative direct tension stress–strain curve for each of the six strain rates investigated in this study is shown in Fig. 2(a). A zoomed view of this figure showing the elastic region, as well as the inelastic stress–strain curve up to 0.2% strain is shown in Fig. 2(b). Although this figure shows an increase in the elastic moduli of dogbones with strain rate, it underestimates the modulus at each strain rate (due to slight slippage at LVDT attachment points), and more accurate measurements with strain gauges are needed to accurately determine the elastic modulus at each strain rate.

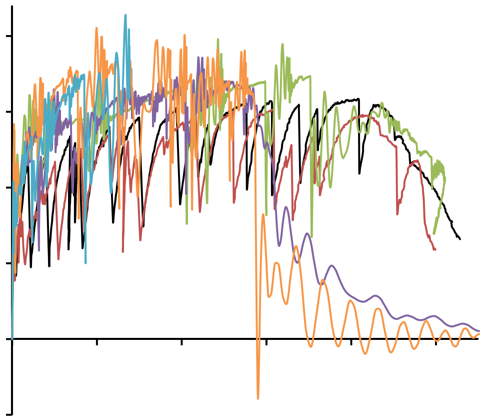

The fluctuations in stress in Fig. 2(a) and (b) are caused by both the formation of matrix micro-cracks and, at high strain rates, by "stress oscillations" as well. As a matrix micro-crack is formed, the sudden decrease of stiffness at that cross-section (due to loss of matrix bridging) causes almost instantaneous reduction of stress [as shown in Fig. 2(b)], which is also observed in the quasi-static stress–strain curve (0.0001/s). In addition, for high strain rates (≥0.01/s), "stress oscillations" are observed (with shallower slopes than the stress drops due to matrix cracking) in Fig. 2(b) caused by significant transient responses of both the material and the test setup. Local oscillations at a crack are expected as the fibers are engaged, post-cracking, with a sudden jolt. However, more significant effect can be due to low inertial mass of the actuator of the dynamic test system, which causes a ringing effect as the feedback loop of the test system dynamically readjusts, and overcompensates, in response to the changing stiffness of the material. Thus, the oscillations must be cleaned by taking local average of the data points (for strain rates ≥ 0.01/s), which is achieved in the curves plotted in Fig. 2(c).

The crack patterns in two dogbone specimens, one tested at the slowest strain rate and the other tested at the fastest strain rate, are shown in Fig. 3, and discussed later in the paper. The multiple cracking of the HSHDC specimen and the shape of the stress–strain curves in Fig. 2 are similar to the quasi-static tensile response described by Ranade et al. [1]. A summary of the relevant tensile properties of all 36 dogbone specimens (6 dogbones for each strain rate) is given in Table 2.

In Table 2, the *first crack strength* (σ_{fc}) refers to the stress at which the first micro-crack occurs in the multiple-cracking HSHDC specimen, observed as the first drop in tensile stress in the curves of Fig. 2(b) right after the elastic stage. The *ultimate tensile strength* (σ_{ult}) refers to the maximum uniaxial tensile stress observed in the averaged curves of Fig. 2(c), and the *tensile strain capacity* is the strain corresponding to the ultimate tensile strength. $PSH_{strength}$ in Table 2 is the strength index for pseudo-strain hardening, mathematically equal to the ratio $\sigma_{ult} / \sigma_{fc}$ [37]. It is a measure of the stress margin available between σ_{fc} and σ_{ult} for forming micro-cracks. Greater $PSH_{strength}$ facilitates more number of micro-cracks. These results of the direct tension tests in terms of average behaviors and variations are discussed below.

The average first crack strength (σ_{fc}) and the average ultimate tensile strength (σ_{ult}) of HSHDC dogbone specimens observed at various strain rates are plotted in Fig. 4. It is observed that both σ_{fc} and σ_{ult} steadily increase with strain rate. From the lowest to the highest strain rate, while σ_{fc} increases by about 53% (8.1 MPa at 0.0001/s to 12.4 MPa to 10/s), σ_{ult} increases by about 42% (14.5 MPa at 0.0001/s to 20.6 MPa to 10/s). The plausible reasoning behind these increases based on the changes in the micro-scale fiber/matrix interaction properties, fiber properties, and matrix fracture toughness is discussed in the next section. As a result of the comparable increases in both σ_{fc} and σ_{ult}, the average strength index for pseudo-strain hardening ($PSH_{strength}$) remains almost constant around 1.8 ($\pm$0.2) at all strain rates (Table 2).

In spite of a relatively constant average $PSH_{strength}$ for various strain rates (which maintains approximately the same number of cracks), the tensile strain capacity decreases with increasing strain rate up to 0.1/s and plateaus thereafter, as observed in Fig. 5. As discussed in the next section, the energy index for pseudo-strain hardening (PSH_{energy}) [37] is well above 1 at all strain rates and, therefore, does not limit steady-state cracking. Given these facts, the observed decrease in the tensile strain capacity of about 31% (ε_{tu} is 4.2% at 0.0001/s and 2.9% at 0.1/s) can be attributed to the corresponding reduction of about 25% in the average residual crack width from 160 μm at 0.0001/s to 120 μm at 0.1/s. Similar to the trend in the tensile strain capacity, the average residual crack width also plateaus after the strain rate of 0.1/s (Fig. 5). The micro-scale rate effects that result in reducing crack widths and, therefore, tensile strain capacities at higher strain rates are discussed in the following section.

For individual dogbone specimens, a positive correlation between $PSH_{strength}$ and tensile strain capacity is observed, regardless of the strain rate. The $PSH_{strength}$ indices of all 36 dogbone specimens are plotted together in Fig. 6. This observation supports the hypothesis that the fundamental principles of micromechanics for achieving or enhancing tensile ductility in HSHDC (and similar materials) are valid regardless of the strain rates.

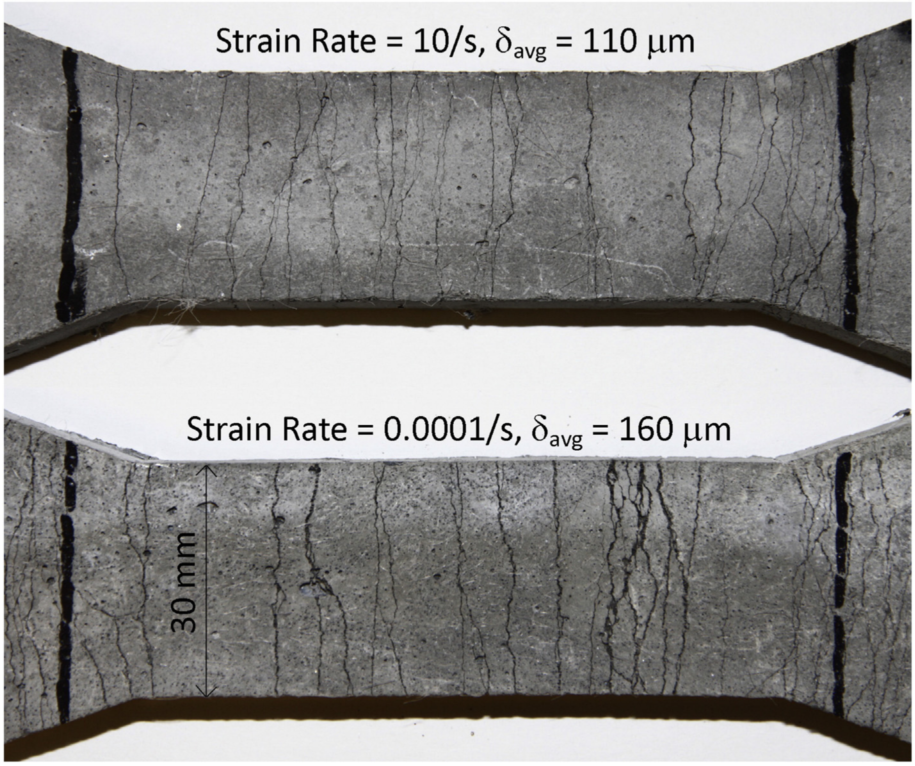

Fig. 3. Influence of strain rates on the crack pattern of dogbone specimens.

All the mechanical properties of the dogbone specimens exhibit an increase in variation, as shown by the standard deviation bars in Figs. 4 and 5, with strain rate. This behavior at the composite scale is caused by a similar increase in variation of micro-scale fiber/matrix interaction properties and matrix fracture toughness with strain rate, as discussed in the next section. In spite of the variation in properties, the minimum tensile ductility among all the 36 HSHDC dogbone specimens is 1.7% at 10/s exhibited by specimen #31.

4.2. Micro-scale response

Representative pullout curves of the single PE fibers embedded in the HSHDC matrix are shown in Fig. 7. This figure not only captures the influence of displacement rate, but also of embedment length and angle of inclination with respect to the loading direction. The description of various phases of these pullout curves is given by Ranade et al. [2]. Also detailed by Ranade et al. [2] are a debond-pullout model (based on the original work by Li and co-workers [38,39]) and methods to extract the underlying fiber/matrix interaction properties of HSHDC, based on these pullout curves. In the following, the rate effects on average fiber/matrix interaction properties as well as fiber properties, deduced from the pullout curves of all 150 specimens (25 for each of the six displacement rates) using the same methods as that used for quasi-static tests by Ranade et al. [2], are reported.

The observed variations of the fiber/matrix interfacial frictional bond (τ_0) and the slip hardening parameter (β) with displacement rate are shown in Fig. 8. τ_0 increases only slightly (by about 14%) over the six orders of displacement rates investigated in this study. This is also apparent in Fig. 7, which shows only a small increase in the peak load of the pullout curve at the fastest displacement rate of 900 mm/s compared to the quasi-static displacement rate of 0.009 mm/s. This observation is consistent with the previous findings of Yang and Li [27] and Maalej et al. [30], who similarly reported relatively weak dependence of τ_0 on the displacement rate. As mentioned in the introduction, the primary cause of rate dependency in FRCCs containing hydrophilic polymer fibers is the fiber/matrix chemical bond. In contrast, the absence of chemical bond between the hydrophobic PE fibers and HSHDC matrix makes the overall interfacial bond less sensitive to rate effects. Slip-hardening which is caused by the matrix-induced fibrillation of the fiber as it pulls out of the matrix tunnel increases the fiber/matrix frictional bond [40]. Although the slip-hardening parameter (β) doubles from 0.003 at 0.009 mm/s to 0.006 at 900 mm/s, it causes an insignificant increase in pullout force, particularly at low slip magnitude (<500 μm). For comparison, β for Engineered Cementitious Composites (ECC – a strain-hardening FRCC) is about 0.6 [41]. These increases in τ_0 and β with displacement rate have relatively minor influence on the bridging behavior of the PE fibers in HSHDC.

The fiber/matrix interaction properties: snubbing coefficient (f) and inclination hardening parameter (μ) (defined by Ranade et al. [2]), both, exhibit rate dependence as observed in Fig. 9. The snubbing effect magnifies the pullout load of an inclined fiber compared to a fiber aligned with the loading direction. This is evident from the pullout curves shown in Fig. 7. In spite of a slightly smaller embedment length, the specimen with the fiber inclined at 45° (green curve) generates significantly greater peak debond load compared to the specimen with aligned fiber (black curve). The influence of the inclination hardening (unique to HSHDC), which only applies in the pullout stage (unlike the snubbing effect), is also observable in Fig. 7 in the post-debond stage of the pullout curves. Further details of both these effects of inclined fibers in HSHDC are presented by Ranade et al. [2].

From Fig. 9, it can be observed that the snubbing coefficient increases by about 27% from the slowest to the fastest displacement rate used in this study. The pullout load is, however, multiplied by $e^{f\phi}$ (modeled as a frictional pulley [42]), which makes the effect of increase in f on the pullout load less than 27%. For instance, for a fiber inclined at angle $\phi = 45°$ with respect to the loading direction, the ratio of the pullout load at high rate to that at quasi-static rate is $e^{\phi(f_{hr}-f_{qs})} = e^{\pi/4(0.75-0.59)} = 1.13$, where f_{hr} and f_{qs} are the snubbing coefficients at displacement rates of (high-rate) 900 mm/s and (quasi-static) 0.009 mm/s, respectively.

This 13% increase in pullout load due to increase in f is supplemented by the change in inclination hardening parameter (μ), which increases

Table 2
Summary of properties of HSHDC dogbone specimens under direct tension.

Strain rate s^{-1}	Specimen no. #	First crack strength σ_{fc} (MPa)	Ultimate tensile strength σ_{ult} (MPa)	$PSH_{strength}$ σ_{ult}/σ_{fc}	Tensile strain capacity ε_{tu} (%)	Average residual crack width δ_{avg} (μm)
0.0001	1	8.6	13.6	1.58	4.3	160
	2	9.1	15.0	1.64	3.7	
	3	6.6	15.6	2.36	4.8	
	4	8.7	13.3	1.53	4.0	
	5	7.5	15.8	2.09	4.7	
	6	8.2	13.5	1.64	3.9	
	Avg.	8.1	14.5	1.8	4.2	
	St. dev.	0.9	1.1	0.3	0.4	
	COV	11%	8%	19%	10%	
0.001	7	7.2	14.3	1.99	3.3	150
	8	6.5	15.9	2.47	4.8	
	9	9.2	14.2	1.54	3.3	
	10	7.7	16.8	2.18	4.2	
	11	8.6	14.9	1.73	3.6	
	12	6.6	15.9	2.39	4.1	
	Avg.	7.6	15.3	2.05	3.9	
	St. dev.	1.1	1.0	0.37	0.6	
	COV	14%	7%	18%	16%	
0.01	13	11.0	17.1	1.55	2.4	140
	14	7.6	17.6	2.32	3.1	
	15	7.2	15.4	2.14	2.8	
	16	9.2	15.2	1.65	3.7	
	17	8.7	17.4	2.01	3.5	
	18	9.8	15.1	1.55	4.5	
	Avg.	8.9	16.3	1.87	3.3	
	St. dev.	1.4	1.2	0.33	0.8	
	COV	16%	7%	18%	23%	
0.1	19	9.7	19.0	1.96	3.1	120
	20	8.2	18.7	2.27	3.7	
	21	10.1	16.9	1.67	3.2	
	22	10.9	18.6	1.70	2.2	
	23	12.7	15.4	1.22	1.9	
	24	6.8	16.1	2.38	3.1	
	Avg.	9.7	17.5	1.87	2.9	
	St. dev.	2.1	1.5	0.43	0.7	
	COV	21%	9%	23%	23%	
1	25	7.4	16.5	2.23	3.9	110
	26	11.6	20.9	1.80	3.7	
	27	8.5	21.6	2.54	3.4	
	28	14.4	20.5	1.42	1.9	
	29	11.8	16.0	1.35	2.3	
	30	12.6	20.2	1.60	2.4	
	Avg.	11.1	19.3	1.82	2.9	
	St. dev.	2.6	2.4	0.47	0.8	
	COV	24%	12%	26%	28%	
10	31	16.0	20.2	1.26	1.7	110
	32	10.6	22.5	2.12	3.6	
	33	11.7	21.5	1.85	2.6	
	34	8.4	16.2	1.93	3.3	
	35	14.6	22.8	1.56	2.2	
	36	13.1	20.5	1.56	2.9	
	Avg.	12.4	20.6	1.71	2.7	
	St. dev.	2.8	2.4	0.31	0.7	
	COV	22%	12%	18%	26%	

from 386 N/(m-rad) at 0.009 mm/s to 553 N/(m-rad) at 900 mm/s (Fig. 9). This increase in μ causes about 43% increase in the inclination hardening contribution (the term $\mu\phi(u - u_0)$ in Eq. (5) of [2]), which is at most 10% of the total pullout load. Therefore, this increase in μ due to displacement rate can cause a maximum increase of about 4.3% (43% times 10%) in the fiber-bridging stress. As both the snubbing and the inclination hardening mechanisms are based on the normal reaction from the matrix [2], these increases in *f* and μ may be caused by the increase in the matrix fracture toughness (detailed below), and strength and modulus of the matrix (similar to effects on other high strength concretes mentioned in the introduction) at high strain rates. Thus, the rate dependencies of *f* and μ are moderately significant for the rate dependence of fiber-bridging in HSHDC.

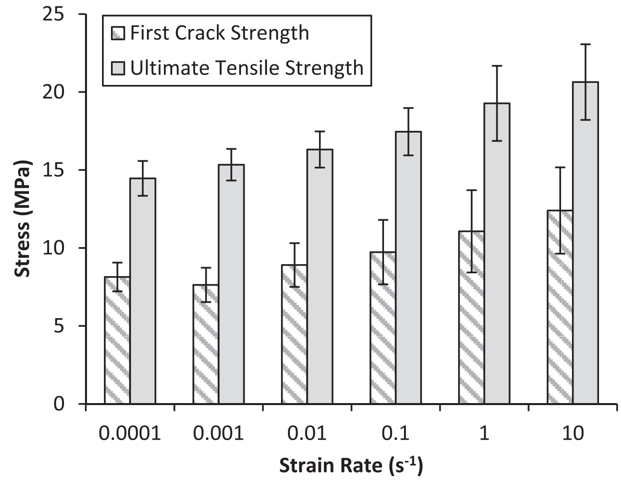

Fig. 4. Rate effects on the strengths of the HSHDC dogbone specimens. Error bars represent one standard deviation.

Rate effects in the PE fiber's in-situ strength and modulus directly influence the fiber-bridging in HSHDC, and are investigated in this study using PE fibers with long embedment lengths (greater than 15 mm) along with the fiber/matrix interaction properties deduced above. Such long embedment length ensures that the fibers reach their breaking strength before completely debonding from the matrix, and it also allows the use of debond-stage equations to compute the in-situ fiber modulus [2]. Polymers, in general, are known to have a viscoelastic behavior, which causes increase in fiber strength and modulus (and brittleness) with increase in strain rate [43,44]. The variations in fiber strength and modulus with displacement rate are plotted in Fig. 10. While the PE fiber strength increases by about 21% of its quasi-static value, the fiber modulus increases by approximately 85% of its quasi-static value. The influence of these increases in fiber strength and modulus on the fiber-bridging curve of HSHDC is discussed in the next section.

Both the necessary conditions of multiple cracking (Eqs. (8) and (9) in [2]) depend as much on the matrix fracture toughness (K_m) as on the fiber-bridging behavior of HSHDC, and therefore, the variation of K_m with the displacement rate is investigated in this study along with the rate effects on the fiber/matrix interaction properties detailed above. The average fracture toughness of HSHDC matrix, as determined from

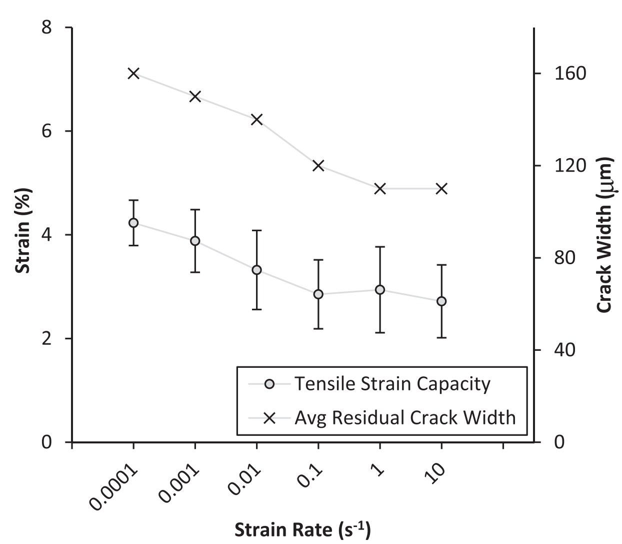

Fig. 5. Rate effects on the tensile strain capacity and average crack width of the HSHDC dogbone specimens. Error bars represent one standard deviation.

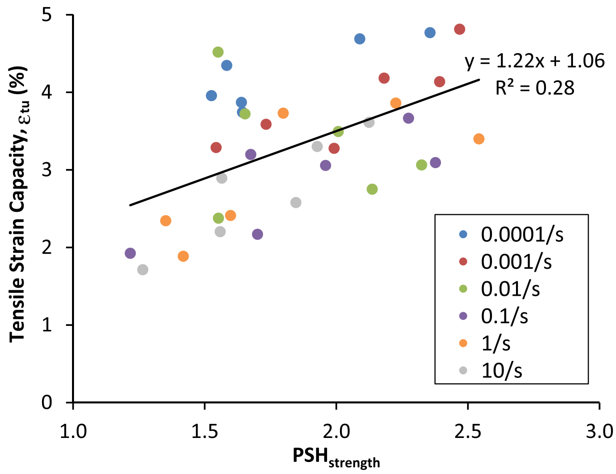

Fig. 6. Correlation between tensile strain capacity and $PSH_{strength}$.

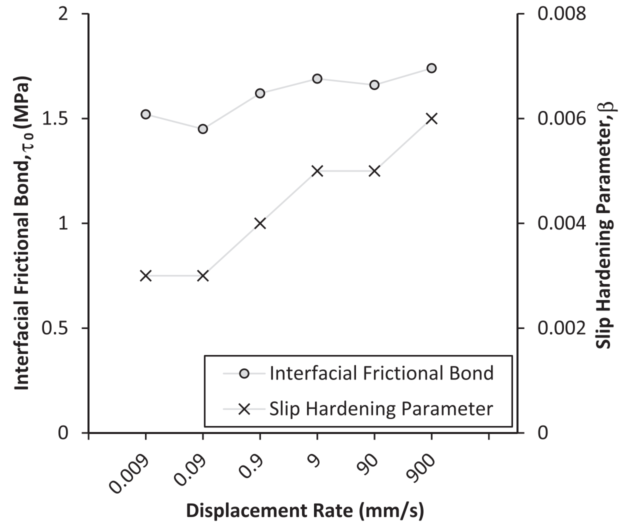

Fig. 8. Rate effects on fiber/matrix interfacial bond properties (τ_0 and β) of HSHDC.

the bend tests on the notched beams, increases from 1.10 MPa√m at 0.02 mm/s to 1.31 MPa√m at 10 mm/s (Fig. 11) (for comparison, the fracture toughness of Ultra-high Performance Concrete (UHPC) matrix (which has similar compressive strength as HSHDC) at quasi-static strain rates is 1.31 MPa√m [45], and that of the ECC (which has the same tensile ductility as HSHDC) matrix at quasi-static strain rates is about 0.5 MPa√m [28]). Unlike the fiber/matrix interaction properties which were measured at six different displacement rates, the matrix fracture toughness was measured only at four different displacement rates up to 10 mm/s due to the limits of the experimental setup as discussed above. This increase in fracture toughness causes a proportional increase in the matrix cracking strength and quadratic increase in the crack tip fracture toughness, which are both detrimental for the pseudo-strain hardening (PSH) indices and tensile ductility [2]; however, as discussed in the next section, the increase in the fiber-bridging capacity and sufficient complementary energy at all strain rates ensures adequate tensile ductility of HSHDC in spite of the increase in matrix fracture toughness at high strain rates.

All the micro-scale properties discussed above exhibit an increase in variation with strain/displacement rates. While the variations in form of standard deviation bars are shown for fiber properties and matrix fracture toughness in Figs. 10 and 11, the variations in the fiber/matrix interaction properties are depicted as coefficient of determination (R^2) values in Fig. 12 (due to the method used to determine these properties [2]). Lower R^2 values imply higher variation in properties, which is the case for all the fiber/matrix interaction properties examined in this study. This increase in the variation of fiber/matrix bond properties at higher displacement rates may be caused by the corresponding increase in variation of fiber and matrix properties at higher displacement rates observed in Figs. 10 and 11.

5. Analytical investigation and comparison with experimental results

In this section, the influence of the micro-scale rate effects on the composite behavior of HSHDC is analytically investigated, and it is determined whether the micro-scale rate effects can quantitatively explain the observed composite-scale rate effects through statistical scale-linking. For this purpose, the measured average values of fiber/matrix interaction properties and fiber properties (reported in the last section) at various strain rates are used to compute an analytical expression, P(u), for single fiber pullout using the debond-pullout model for HSHDC given by Ranade et al. [2]. This analytical expression describes the pullout force, P, as a function of the relative displacement, u, for a given embedment length (z) and orientation angle (ϕ) with respect to the loading direction, which models the observed P-u relations plotted in Fig. 7. However, a micro-crack in HSHDC is bridged by numerous

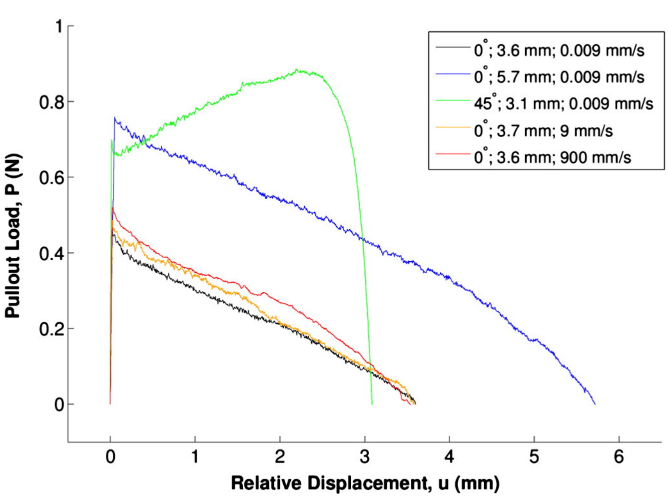

Fig. 7. Experimentally determined representative pullout curves of PE fibers embedded in HSHDC matrix. Legend: Inclination angle with respect to the loading direction; fiber embedment length; displacement rate.

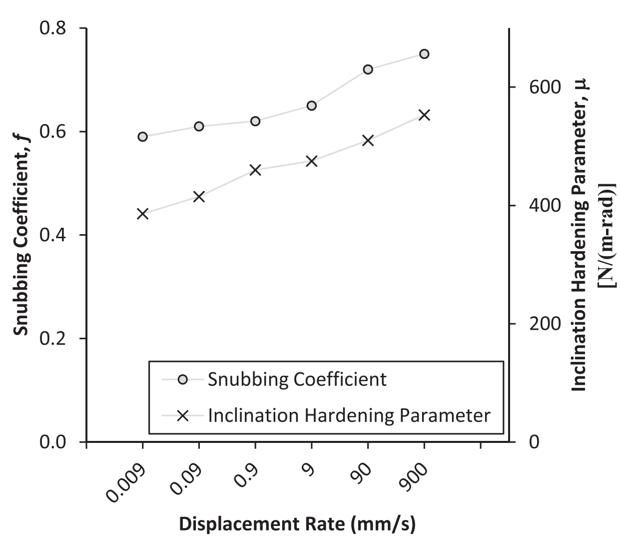

Fig. 9. Rate effects on fiber/matrix interaction properties (*f* and μ) of HSHDC.

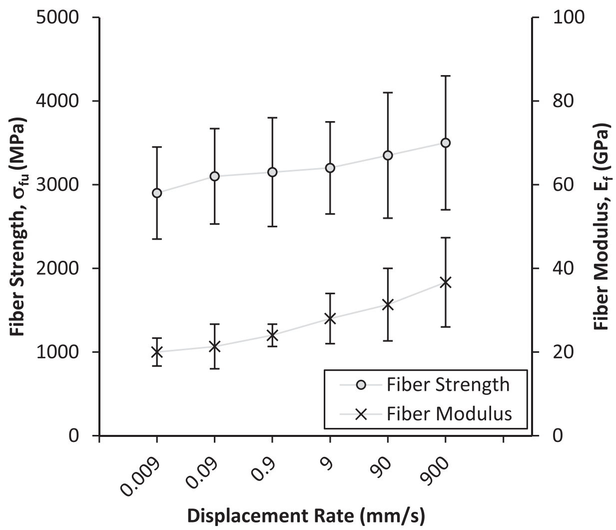

Fig. 10. Rate effects on PE fiber properties. Error bars represent one standard deviation.

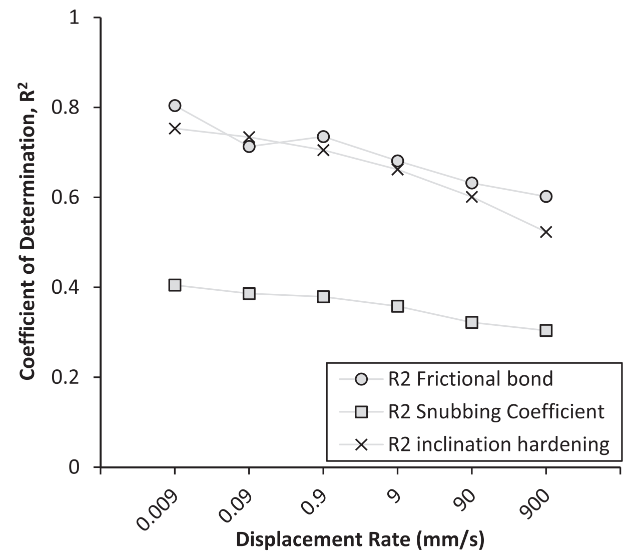

Fig. 12. Rate effects on variation in fiber/matrix interaction properties determination.

fibers with random embedment lengths and orientations, as schematically shown in Fig. 13. The total fiber-bridging stress (σ) across a crack for a given opening (δ) (also called fiber-bridging or σ–δ relation) is obtained by integrating the force contributions from all the fibers bridging across the crack using a statistical scale-linking model described by Eq. (1) [39].

$$\sigma(\delta) = \frac{V_f}{A_f}\int_0^{\pi/2}\int_0^{(L_f/2)\cos(\phi)} P(u)p(z)p(\phi)dzd\phi \quad (1)$$

In Eq. (1), the number of fibers of every possible embedment length and orientation angle with respect to the loading direction is counted using the probability density functions, $p(z)$ and $p(\phi)$ respectively, determined through the observations of HSHDC specimen cross-sections [2]. Furthermore, V_f is the fiber volume fraction (equal to 2%) in HSHDC and A_f is the cross-sectional area of the PE fiber. Thus, all the above micro-scale parameters are used as inputs in Eq. (1) to compute the fiber-bridging relations of HSHDC at various strain rates, which are directly related to the composite tensile response of HSHDC, as discussed below.

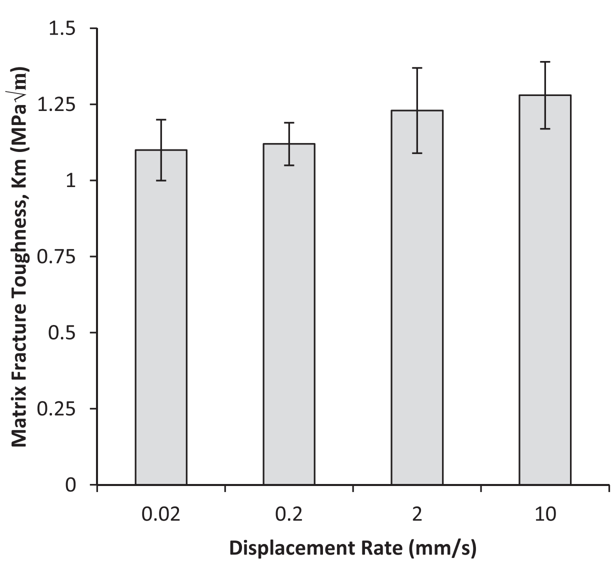

Fig. 11. Rate effects on matrix fracture toughness. Error bars represent one standard deviation. 1 MPa√m is equivalent to a peak load of 1592 N on a notched beam specimen of size: span = 10″; depth = 3″; width = 1.5″, and notch length of 1.2″.

The results of the scale-linking analysis in the form of computed fiber-bridging (σ-δ) curves of HSHDC at various displacement rates (corresponding to the strain rates for the dogbone testing) are plotted in Fig. 14. While the increase in the fiber modulus at high displacement rates increases the rising slope (*fiber-bridging stiffness*, $d\sigma^+/d\delta$) of the σ–δ curve, the increase in fiber's strength causes an increase in the peak of the σ–δ curve (*fiber-bridging capacity*, σ_0). Furthermore, the increases in the fiber/matrix interaction properties (τ_0, β, f, and μ) increase both, the fiber-bridging stiffness as well as the fiber-bridging capacity, at high displacement rates. As a result, it is observed in Fig. 14 that, with increasing displacement rate, both the rising slope and the peak of the computed σ–δ curve increase.

The computed fiber-bridging curves can be used to approximately estimate the ultimate tensile strength and average crack width of the HSHDC dogbone specimens at various strain rates. As explained by Ranade et al. [2], different cross-sections of the HSHDC dogbone specimens contain different numbers of fibers due to inhomogeneous dispersion of fibers during the mixing process. Thus, while the *average* σ–δ curves shown in Fig. 14 are computed for average fiber volume fraction (V_f) of 2%, the volume fraction at a real HSHDC specimen cross-section will almost never be equal to 2%. As the fiber-bridging capacity (σ_0) across a cracked cross-section is directly proportional to V_f [Eq. (1)] at that section, the cracked cross-section of the dogbone specimen containing the least number of fibers [$\min(V_f)$], among all the other cracked

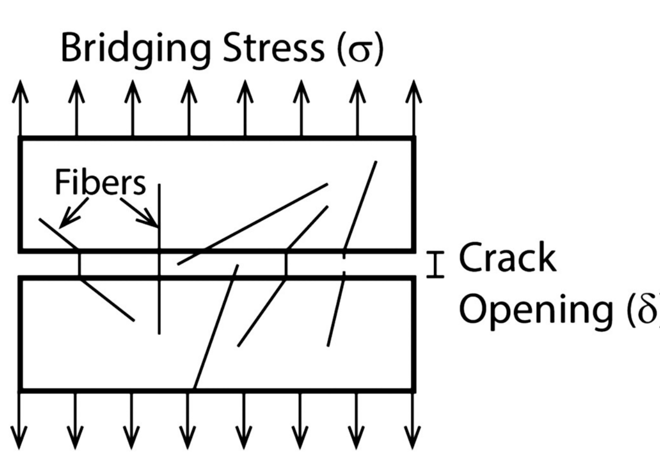

Fig. 13. Schematic representation of fibers with random orientations and embedment lengths bridging across a micro-crack in HSHDC.

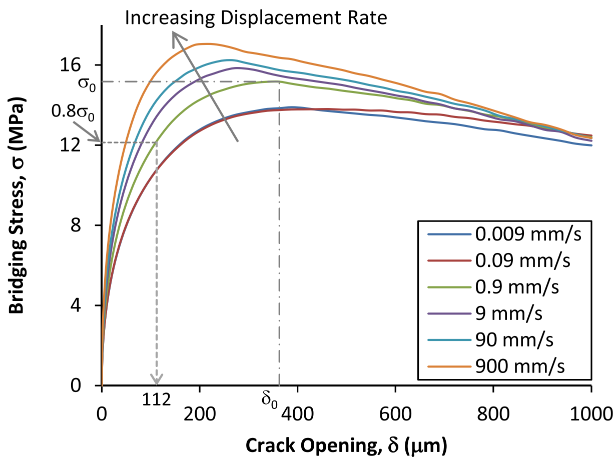

Fig. 14. Computed fiber-bridging (σ-δ) relations for HSHDC at various displacement rates.

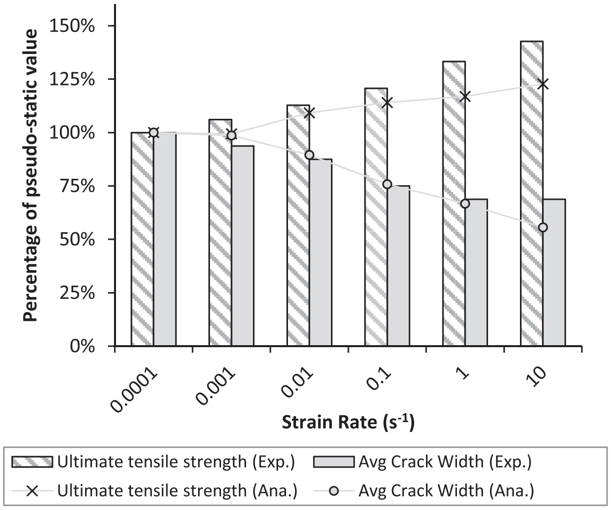

Fig. 15. Comparison of experimentally observed (Exp.) and analytically predicted (Ana.) rate effects on the tensile properties of HSHDC.

cross-sections of that specimen, is also likely to have the minimum fiber-bridging capacity, min(σ_0). Furthermore, as equal tensile stress must be transferred across all the cross-sections of the dogbone due to equilibrium, the ultimate tensile strength of the dogbone specimen is theoretically equal to min(σ_0). Additionally, the crack opening (δ) corresponding to the min(σ_0) on the average σ–δ curve (plotted in Fig. 14) is the expected value of the average crack width (δ_{avg}) of the dogbone specimen [2]. This method, proposed in Yang et al. [46], for estimating the ultimate tensile strength and average crack width from the average σ–δ curve is further explained below with a sample calculation.

As an example, consider the computed σ–δ curve corresponding to the displacement rate of 0.9 mm/s. As marked in Fig. 14, the peak of this curve or the fiber-bridging capacity (σ_0) is equal to 15.2 MPa. The min(V_f) was determined equal to 0.80 times 2% from a statistical analysis (average minus two standard deviations) of the fiber distributions observed using fluorescence microscopy at multiple cross-sections of HSHDC specimens [2]. Therefore, the min(σ_0) is equal to 0.8 times 15.2 MPa equal to 12.2 MPa, and the corresponding crack opening is 112 μm as shown in Fig. 14.

Due to the statistical method used to determine min(V_f), the computed min(σ_0) of 12.2 MPa is the lower bound for the average ultimate tensile strength capacity of the dogbone specimens at the displacement rate of 0.9 mm/s. As a result, both the ultimate tensile strength [min(σ_0)] and the corresponding crack width (112 μm) predicted by this method at the displacement rate of 0.9 mm/s are less than the experimentally determined values (Table 2) from the direct tension tests on the dogbone specimens at the corresponding strain rate of 0.01/s. Nevertheless, taking the ratio of the ultimate tensile strengths (or crack widths) at any two strain rates minimizes the influence of V_f as σ_0 is linearly proportional to V_f. Therefore, in the following discussion comparing the predicted rate effects versus the observed rate effects at the composite scale, the ratios of properties, instead of the absolute values of those properties, at a given strain rate relative to the properties at the quasi-static strain rate are used.

By a similar analysis of all the σ–δ curves in Fig. 14, the ultimate tensile strength and average crack widths are estimated for equivalent strain rates and are plotted in Fig. 15 along with the experimental results of the direct tension tests performed on the HSHDC dogbone specimens. In this figure, as mentioned above, instead of the absolute values of the ultimate tensile strengths and crack widths, percentages relative to the 'respective' quasi-static values are plotted to capture the rate effect. 'Respective' quasi-static values at strain rate of 0.0001/s are: (1) Ultimate tensile strength (Experimental) = 14.5 MPa (Fig. 4), (2) Ultimate tensile strength (Analytical) = 11.3 MPa (Fig. 14), (3) Average (residual) crack width (Experimental) = 160 μm (Figs. 5), and (4) Average crack width (Analytical) = 140 μm (Fig. 14). The comparison of the analytically estimated and experimentally observed changes in crack widths and ultimate tensile strength is discussed below.

As observed in Fig. 15, the experimentally determined crack width reduction with increasing strain rates is well estimated (with difference of less than 5%) by the scale-linking analysis, particularly for the strain rates up to 1/s. The significant increase in the fiber modulus, assisted by the slight increase in fiber/matrix interfacial frictional bond, causes an increase in the fiber-bridging stiffness which explains the observed crack width reduction. It should be noted that although the fiber modulus increases by about 57% as the strain rate is increased from 0.0001/s to 1/s, the estimated reduction in crack width is only 33%. This is because, for the same change in the strain rate, the fiber strength only increases by about 15%, which increases the fiber breakage at high strain rates and reduces the slope of the σ–δ curve, particularly near its peak. At the strain rate of 10/s, the difference between the experimental and analytical values increases; while the analytical model estimates the average crack width to be 56% of its quasi-static value, the experimental observation shows that the crack width reduces to 69% of its quasi-static value.

In Fig. 15, the ultimate tensile strength change is also well predicted by the analytical model, particularly for strain rates up to 0.1/s. The increase in the strength of the fiber, assisted by the slight increase in fiber/matrix interfacial frictional bond, increases the fiber-bridging capacity which explains the observed increase in the ultimate tensile strength of HSHDC dogbone specimens. Compared to the errors at low strain rates (less than 7%), the errors between the analytical and experimental values are greater at the highest two strain rates of 1/s and 10/s. Overall, a good match is observed in Fig. 15 between analytically estimated and experimentally observed rate effects on the ultimate tensile strength and average crack width, albeit with greater discrepancy at the two highest strain rates.

As the composite-scale properties are closely related to the microscale properties, the lack of agreement between the experimental and analytical values at the highest two strain rates may be due to the significant increase in the variation of fiber/matrix interaction properties (Fig. 12) and fiber properties (Fig. 10) at these two strain rates. In addition, the possibility of unknown hardening mechanisms at these two very high strain rates cannot be ruled out due to the complex behavior of cementitious materials, particularly at high strain rates.

The increase in the average matrix fracture toughness with strain rate is compared with that of average first crack strength of HSHDC dogbone specimens in Fig. 16. As all the specimens belong to the same batch of material, the maximum flaw size is expected to be approximately similar in all specimens regardless of the strain rate. It is

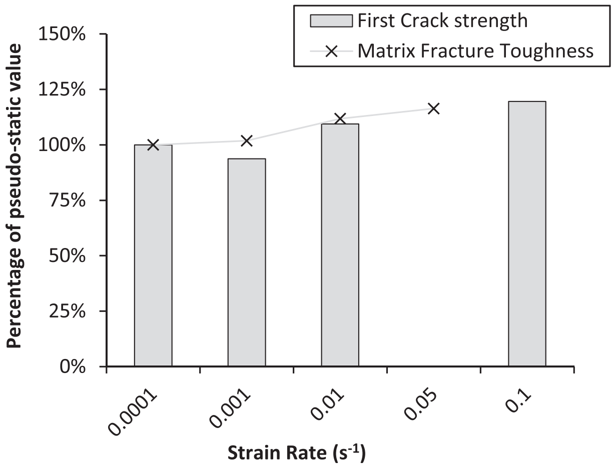

Fig. 16. Comparison of observed rate effects in first crack strength of HSHDC composite specimens and matrix fracture toughness.

observed in Fig. 16 that the first crack strength closely follows the trend in the matrix fracture toughness, which is expected from the Irwin's fracture criterion.

In addition to estimating the ultimate tensile strength and average crack width in HSHDC, the computed fiber-bridging (σ–δ) curves in Fig. 14 are also used to estimate the complementary energy of fiber-bridging (J_b'), whose comparison with the crack tip toughness (J_{tip}) determines the feasibility of steady-state cracking (which facilitates tensile ductility) in HSHDC at high strain rates. J_b' is computed as the external work done during steady-state crack propagation (the product $\sigma_0.\delta_0$) less that absorbed by the bridging fibers near the crack tip as the crack opens up to δ_0 (area under the σ–δ curve before δ_0). Here, δ_0 is the crack opening corresponding to the fiber-bridging capacity (σ_0) as shown in Fig. 14. Due to steeper σ–δ curves, J_b' reduces at the highest displacement rate to about 600 J/m^2 from 969 J/m^2 at the quasi-static rate. J_{tip} is estimated approximately equal to K_m^2/E_c [2], where K_m is the matrix fracture toughness given in Fig. 11 and E_c is the tensile modulus of HSHDC taken as 48.4 GPa [1]. As mentioned in Section 3.2, K_m could not be computed at the highest strain rate due to the limitations of the experimental setup. Conservatively assuming that K_m doubles and E_c remains constant, J_{tip} would increase from 25 J/m^2 at the quasi-static strain rate to 100 J/m^2 at the highest strain rate investigated in this study. Thus, in spite of the increase in the matrix fracture toughness, J_{tip} remains significantly smaller than J_b' even at high strain rates, which coupled with constant σ_{ult}/σ_{fc} ratio (due to comparable increases in matrix fracture toughness and fiber-bridging capacity) facilitates multiple cracking at all strain rates investigated in this study.

6. Summary and conclusions

The tensile strain rate effects on the composite and micro-scale properties of a newly developed FRCC, called High Strength-High Ductility Concrete, were experimentally investigated. Analytical scale-linking model was used to explain and understand the composite-scale rate effects based on the micro-scale rate effects. As a result, new insights into the material behavior were developed, which will be useful for the continued development of this unique composite for enhancing structural resilience under extreme loading. The following conclusions can be drawn.

- *Composite-scale rate effects under direct tension*: As the strain rate is increased from 0.0001/s to 10/s, average first crack strength (σ_{fc}) and average ultimate tensile strength (σ_{ult}) of HSHDC dogbone specimens increase by about 53% and 42%, respectively. In spite of a relatively constant ratio of σ_{ult}/σ_{fc} with strain rate, the tensile strain capacity decreases with increasing strain rate from about 4.2% at 0.0001/s to 2.9% at 0.1/s and plateaus after that. Such variation in tensile strain capacity is attributable to a similar trend in average crack width which reduces from 160 μm at 0.0001/s to 120 μm at 0.1/s and plateaus for higher strain rates.
- *Micro-scale rate effects*: Almost all the fiber/matrix interaction properties, fiber properties, and matrix fracture toughness exhibit changes with displacement rate (equivalent to the strain rate in composite testing) to varying degrees. The interfacial frictional bond (τ_0) increases only slightly (by 14%) over the six orders of displacement rates investigated in this study (0.009 mm/s to 900 mm/s). Although the slip hardening parameter (β) doubles from 0.003 at 0.009 mm/s to 0.006 at 900 mm/s, it causes an insignificant increase in pullout force, particularly at low slip (<500 μm). The absence of chemical bond between the PE fiber and HSHDC matrix makes the overall fiber/matrix bond relatively insensitive to rate effects. Snubbing coefficient (f) and inclination hardening parameter (μ) increase by about 27% and 43%, respectively, which are determined to be moderately significant for the fiber-bridging in HSHDC. The changes that are the most consequential for fiber-bridging in HSHDC are the increases in PE fiber strength and modulus with displacement rate. At the fastest rate, the PE fiber strength and modulus increase by about 21% and 85% of their respective quasi-static values. However, these increases in fiber strength and modulus, along with the increase in fiber/matrix interaction properties, result in the reduction of complementary energy (J_b') of fiber-bridging. Nevertheless, J_b' remains significantly greater (about 6 times) than the crack tip toughness even at the highest strain rate investigated in this study, which coupled with constant σ_{ult}/σ_{fc} ratio (due to comparable increases in matrix fracture toughness and fiber-bridging capacity) facilitates multiple cracking in HSHDC at all strain rates investigated in this study.
- *Scale-linking*: The scale-linking analysis shows that the micro-scale rate effects satisfactorily explain the rate dependencies at the composite scale. The increase in matrix fracture toughness corresponds well with the increase in first crack strengths at composite-scale. The increases in fiber/matrix interaction properties, and fiber strength and modulus justify the increase in ultimate tensile strength and decrease in average crack width, and therefore tensile strain capacity, with the strain rate.

Acknowledgments

This research at the University of Michigan was supported by a research contract (W912HZ-08-C-0056) from the U.S. Army ERDC, Vicksburg, MS. Helpful discussions with T. Rushing, T. Slawson, B. Williams, and J. Davis of ERDC are gratefully acknowledged. The authors also acknowledge the material suppliers Honeywell, Lafarge, US Silica, Elkem, and WR Grace, for providing materials for this research. Permission to publish was granted by the Director, Geotechnical and Structures Laboratory at ERDC.

References

[1] R. Ranade, V.C. Li, M.D. Stults, W.F. Heard, T.S. Rushing, Composite mechanical properties of high strength-high ductility concrete, ACI Mater. J. 110 (2013) 413–422.
[2] R. Ranade, V.C. Li, M.D. Stults, T.S. Rushing, J. Roth, W.F. Heard, Micromechanics of high strength-high ductility concrete, ACI Mater. J. 110 (2013) 375–384.
[3] W.L. Cowell, Dynamic properties of plain portland cement concrete, Technical Report R447, Naval Civil Engineering Laboratory, Port Hueneme, CA, 1966.
[4] F.M. Mellinger, D.L. Birkimer, Measurement of stress and strain on cylindrical test specimens of rock and concrete under impact loading, Technical Report 4-46, US Army Corps of Engineers, Cincinnati, OH, 1966, pp. 15–22.
[5] D.L. Birkimer, R. Lindemann, Dynamic tensile strength of concrete materials, ACI J. Proc. 68 (1971) 47–49.
[6] J. Takeda, H. Tachikawa, Deformation and fracture of concrete subjected to dynamic load, Proceedings of the International Conference on Mechanical Behavior of Materials, 1972, pp. 267–277.

[7] H.A. Kormeling, A.J. Zielinski, H.W. Reinhardt, Experiments on concrete under single and repeated uniaxial impact tensile loading, Stevin Report 5-80-3, TU Delft, Netherlands, 1980.
[8] M.K. McVay, Spall damage of concrete structures, technical report SL-88-22, US Army Corps of Engineers, Vicksburg, MS, 1988. 95–137.
[9] J. Weerheijm, H.W. Reinhardt, Modelling of concrete fracture under dynamic tensile loading, Proceedings of the Symposium on Recent Developments in the Fracture of Concrete and Rock, Cardiff, Wales, September, 1989.
[10] P.H. Bischoff, S.H. Perry, Compressive behavior of concrete at high strain rates, Mater. Struct. 24 (1991) 425–450.
[11] D. Chandra, A fracture mechanics based constitutive model for concrete under high loading rates, Civil Engineering, Pennsylvania State University, USA, 1993, pp. 7–44.
[12] J.W. Tedesco, C.A. Ross, S.T. Kuennen, Experimental and numerical analysis of high strain rate splitting-tensile tests, ACI Mater. J. 90 (1993) 162–169.
[13] S. Nemat-Nasser, H. Deng, Strain-rate effect on brittle failure in compression, Acta Metall. Mater. 42 (1994) 1013–1024.
[14] L.J. Malvar, J.E. Crawford, Dynamic increase factors for concrete, Proceedings of the 28th DDESB Seminar, Orlando, FL, USA, 1998.
[15] International federation for structural concrete, stress and strain rate effects, Model Code 2010 — First Complete Draft, vol. 1, 2010, pp. 153–156 (Lausanne, Switzerland).
[16] S. Wang, M.H. Zhang, S.T. Quek, Effect of high strain rate loading on compressive behavior of fiber-reinforced high-strength concrete, Mag. Concr. Res. 63 (2011) 813–827.
[17] B. Riisgaard, T. Ngo, P. Mendis, C.T. Georgakis, H. Stang, Dynamic Increase factors for high performance concrete in compression using split Hopkinson pressure bar, Proceedings of the 6th International Conference on Fracture Mechanics of Concrete and Concrete Structures, Catania, Italy, 2007.
[18] A.N. Stroh, A theory of the fracture of metals, Adv. Phys. 6 (1957) 418–465.
[19] C.A. Ross, J.W. Tedesco, S.T. Kuennen, Effects of strain rate on concrete strength, ACI Mater. J. 92 (1995) 37–47.
[20] ACI Committee 446 Subcommittee IV, Report on Dynamic Fracture of Concrete — ACI 446.4R-04, American Concrete Institute, Farmington Hills, MI, 2004.
[21] A.J. Zielinski, Model for tensile fracture of concrete at high rates of loading, Cem. Concr. Res. 14 (1984) 215–224.
[22] H.W. Reinhardt, Strain rate effects on the tensile strength of concrete as predicted by thermodynamic and fracture mechanics models, in: S. Mindess, S.P. Shah (Eds.), Mater Res Soc Symp P, 1985, pp. 1–13.
[23] Z.P. Bazant, J. Planas, Effect of time, environment, and fatigue, Fracture and Size Effect in Concrete and Other Quasibrittle Materials, CRC Press, Washington DC, 1998, pp. 388–398.
[24] H. Mihashi, F.H. Wittmann, Stochastic approach to study the influence of rate of loading on strength of concrete, HERON 25 (1980) 1–55.
[25] G.G. Nammur, A.E. Naaman, Strain rate effects on tensile properties of fiber reinforced concrete, in: S. Mindess, S.P. Shah (Eds.), Mater. Res. Soc. Symp. Proc., 1986, pp. 97–118.
[26] H.A. Kormeling, H.W. Reinhardt, Strain rate effects on steel fiber concrete in uniaxial tension, Cement Concr. Compos. 9 (1987) 197–204.
[27] E.H. Yang, V.C. Li, Rate dependence in engineered cementitious composites, RILEM Workshop on HPFRCC in Structural Applications, Honululu, Hawaii, 2005, pp. 83–92.
[28] E.H. Yang, Designing Added Functions in Engineered Cementitious Composites, Civil Engineering, University of Michigan, Ann Arbor, 2008.
[29] V. Mechtcherine, F.D. Silva, M. Butler, D. Zhu, B. Mobasher, Fracture behavior of HPFRCCs under dynamic tensile loads, in: V. Mechtcherine, M. Kaliske (Eds.), European Conference on Fracture — ECF 18, Dresden, Germany, 2010.
[30] M. Maalej, S.T. Quek, J. Zhang, Behavior of hybrid-fiber engineered cementitious composites subjected to dynamic tensile loading and projectile impact, J. Mater. Civil Eng. 17 (2005) 143–152.
[31] D.J. Kim, Strain Rate Effect on High Performance Fiber Reinforced Cementitious Composites using Slip Hardening High Strength Deformed Steel Fibers, Civil Engineering, University of Michigan, Ann Arbor, 2009.
[32] D.J. Kim, S. El-Tawil, A.E. Naaman, Loading rate effect on pullout behavior of deformed steel fibers, ACI Mater. J. 105 (2008) 576–584.
[33] P. Rossi, E. Parant, Damage mechanisms analysis of a multi-scale fibre reinforced cement-based composite subjected to impact and fatigue loading conditions, Cem. Concr. Res. 38 (2008) 413–421.
[34] U.N. Gokoz, A.E. Naaman, Effect of strain-rate on the pull-out behavior of fibres in mortar, Cement Concr. Compos. 3 (1981) 187–202.
[35] W.G. Knauss, I. Emri, H. Lu, Mechanics of polymers: viscoelasticity, in: W.N. Sharpe (Ed.), Handbook of Experimental Solid Mechanics, Springer, United States, 2008, pp. 49–96.
[36] M.D. Stults, R. Ranade, V.C. Li, T.S. Rushing, Mechanical effects of rice husk ash in ultra-high performance concretes: a matrix study, Advances in Cement-Based Materials, CRC Press/Balkema, 2010, pp. 307–312.
[37] T. Kanda, V.C. Li, Multiple cracking sequence and saturation in fiber reinforced cementitious composites, J. Concr. Res. Technol. 9 (1998) 19–33.
[38] Z. Lin, T. Kanda, V.C. Li, On interface property characterization and performance of fiber reinforced cementitious composites, Concr. Sci. Eng. 1 (1999).
[39] V.C. Li, Y. Wang, S. Backer, A micromechanical model of tension-softening and bridging toughening of short random fiber reinforced brittle matrix composites, J. Mech. Phys. Solids 39 (1991) 607–625.
[40] V.C. Li, S. Wang, C. Wu, Tensile strain-hardening behavior of PVA-ECC, ACI Mater. J. 98 (2001) 483–492.
[41] S. Wang, V.C. Li, Engineered cementitious composites with high-volume fly ash, ACI Mater. J. 104 (2007) 233–241.
[42] V.C. Li, Y. Wang, S. Backer, Effect of inclining angle, bundling and surface treatment on synthetic fibre pullout from cement matrix, Compos. Part A 20 (1990) 132–140.
[43] T. Peijs, E.A.M. Smets, L.E. Govaert, Strain rate and temperature effects on energy absorption of polyethylene fibers and composites, Appl. Compos. Mater. 1 (1994) 35–54.
[44] G.C. Jacob, J.M. Starbuck, J.F. Fellers, S. Simunovic, R.G. Boeman, Strain rate effects on the mechanical properties of polymer composite materials, J. Appl. Polym. Sci. 94 (2004) 296–301.
[45] G. Orange, J. Dugat, P. Acker, Ductal®: new ultra high performance concretes damage resistance and micromechanical analysis, in: P. Rossi, G. Chanvillard (Eds.), Proceedings of Fifth RILEM Symposium on Fiber-Reinforced Concretes (FRC) - BEFIB, 2000, pp. 781–790.
[46] E.H. Yang, S. Wang, Y. Yang, V.C. Li, Fiber-bridging constitutive law of engineered cementitious composites, J. Adv. Concr. Technol. 6 (2008) 1–13.